GSA Data Repository 2018289

Ruh et al., 2018, Shale-related minibasins atop a massive olistostrome in an active accretionary wedge setting: Two-dimensional numerical modeling applied to the Iranian Makran: Geology, https://doi.org/10.1130/G40316.1.

Supplementary Material — Numerical model

Governing equations

The numerical code is written in MATLAB® based on a textbook by Gerya (2010). The finite difference code (fully staggered grid) includes a marker-in-cell Lagrangian marker field. The mechanical model solves for the equations for conservation of mass (incompressible)

$$\frac{\partial u_i}{\partial x_i} = 0 \qquad (1.1)$$

and conservation of momentum (Stokes equation)

$$\frac{-\partial P}{\partial x_i} + \frac{\partial \tau_{ij}}{\partial x_j} = \rho g_i. \qquad (1.2)$$

P denotes mean stress, u_i are velocities, x_i spatial coordinates, τ_{ij} deviatoric stress tensor, ρ density, and g_i is the gravitational acceleration.

Governing equations are discretized on a non-deformable Eulerian grid and solved with the MATLAB's "backslash" direct solver for the two velocity components and dynamic pressure. Material properties are interpolated on freely moving Lagrangian markers that advect through the fixed Eulerian grid according to a fourth-order Runge-Kutta derived velocity field.

Rheological model

The implemented visco-elastic relation between stress and strain rate follows a Maxwell-type form

$$\dot{\varepsilon}_{ij} = \frac{1}{2\eta}\tau_{ij} + \frac{1}{2G}\frac{D\tau_{ij}}{Dt} \qquad (1.3)$$

composed of a viscous and an elastic strain rate part, where G (100 GPa for all marker types in all simulations) indicates the shear modulus and η the effective viscosity with lower and upper cutoffs of 10^{17} and 10^{24} Pa·s, respectively. As described in Gerya (2010), elasticity is implemented by modifying the effective viscosity depending on the applied "computational" time step and the stress history. The objective co-rotational time derivate of visco-elastic stresses is discretized as a function after applying first-order finite difference

$$\frac{D\tau_{ij}}{Dt} = \frac{\tau_{ij} - \tau_{ij}^{old}}{\Delta t} \quad (1.4)$$

where

$$\tau_{ij} = 2\eta\dot{\varepsilon}_{ij}Z + \tau_{ij}^{old}(1 - Z) \quad (1.5)$$

and the visco-elasticity factor

$$Z = \frac{\Delta t \cdot G}{\eta + \Delta t \cdot G} \quad (1.6)$$

with η as effective viscosity, which leads to numerical viscosity

$$\eta_{num} = \eta \cdot Z = \frac{\eta \cdot \Delta t \cdot G}{\eta + \Delta t \cdot G} \quad (1.7)$$

used to solve the set of equations.

Plastic failure occurs if the visco-elastic differential stresses exceed the yield stress ($F > 0$):

$$F = \sigma_{II} - \sigma_y \quad (1.8)$$

where yield stresses σ_y are formulated by the Drucker-Prager yield criterion

$$\sigma_y = P \cdot (1 - \lambda) \cdot \sin\varphi + C \cdot \cos\varphi \quad (1.9)$$

where C is cohesion, φ the friction angle, and λ the fluid pressure ratio of the material. Then, the exceeded stresses are kept within the failure envelope

$$\sigma_{xx}^{new} = \sigma_{xx}\frac{\sigma_y}{\sigma_{II}} \quad (1.10)$$

$$\sigma_{xy}^{new} = \sigma_{xy}\frac{\sigma_y}{\sigma_{II}}. \quad (1.11)$$

and effective viscosity η is reduced to maintain those stresses

$$\eta = \frac{\sigma_y}{2\dot{\varepsilon}_{II}} \quad (1.12)$$

where

$$\dot{\varepsilon}_{II} = \sqrt{\frac{1}{2}\dot{\varepsilon}_{ij}^2}. \quad (1.13)$$

After interpolation of the Eulerian velocity field onto the Lagrangian markers, stress changes and plasticity are calculated on those. The updated effective viscosity is then interpolated back on the Eulerian nodes and used to solve the system of equations. Here, Picard iterations (repeated cycles of global solution) are performed until the maximal nodal velocity change is smaller than 10^{-14} m/s (≈3.2 μm/yr). Time steps exhibit 1000 yr.

Model setup

The Eulerian model box scaled as 200 km horizontal length to 20 km vertical thickness (Fig. S1). An initially 4.5 km thick pre-olistostrome sequence including a basal and an intermediate décollement as in the Makran accretionary wedge (Ruh et al., 2012) is accreted by pulling out the base below a rigid and fixed backstop. The gravitational force is tilted by 1° to the vertical axis of the model box, mimicking the low-angle inclination of the wedge base towards the backstop (Davis et al. 1983).

Material properties

Rheological information is stored on Lagrangian markers (9 markers per Eulerian cell) that advect accordingly to the Eulerian velocity field. Rock markers have an initial viscosity of 10^{24} Pa·s, an elastic shear modulus of 10^{11} Pa, and a constant density of 2700 kg/m^3. “Sticky-air” has a constant viscosity of 10^{17} Pa·s and a density of 1000 kg/m^3 or 1 kg/m^3, for water or air, respectively. The sedimentary sequence has a friction angle of 30°

and an initial cohesion of 1 MPa, which are lowered linearly to 25° and 0.1 MPa, respectively, between an accumulated plastic strain of 0.5 and 1.5 (Ruh et al., 2014), which mimics the loss of cohesion during brittle fracturing (Zhang et al., 2015). The décollements have friction angles of 10° (basal) and 5° (intermediate) and a cohesion of 0.1 MPa, without any strain weakening applied. Syn-tectonic sedimentation during wedge growth is modelled by a linear diffusion scheme

$$\frac{\partial h_s}{\partial t} = \kappa \frac{\partial^2 h_s}{\partial x_i^2} \qquad (1.14)$$

where erosion takes place above the sea level and sedimentation below. Post-olistostrome syn-tectonic sediments have equal strength properties as the initial sequence and a density of 2500 kg/m^3.

The reference model olistostrome has a viscosity of 10^{19} Pa·s and a density of 2000 kg/m^3, and a diffusion coefficient of 10^{-6} m^2/s acting as a surface process, where only sedimentation occurs below sea level, and only erosion above sea level. Further experiments are obtained to test the effects of varying viscosity and density of the olistostrome, and the influence of surface diffusion on the system (Table S1,S2, Figure S2-S15).

Boundary conditions

The applied lateral velocity boundary conditions resemble those of an analogue sandbox model. The lower boundary has no vertical velocity induced and a left-directed velocity of 1 cm/yr. The left side is a rigid no-slip boundary, acting as a backstop. On the right model side, markers enter to Eulerian box with a velocity of 1 cm/yr and free-slip is applied vertically. The top has a free-slip boundary that compensates for the incoming material to the right with a vertical velocity of 0.1 cm/yr.

Gerya, T., 2010. Introduction to Numerical Geodynamic Modelling. Cambridge University Press.

Ruh, J.B., Gerya, T., Burg, J.P., 2014. 3D effects of strain vs. velocity weakening on deformation patterns in accretionary wedges. Tectonophysics 615, 122-141.

Ruh, J.B., Kaus, B.J.P., Burg, J.P., 2012. Numerical investigation of deformation mechanics in fold-and-thrust belts: Influence of rheology of single and multiple décollements. Tectonics 31.

Zhang, H.Q., Tannant, D.D., Jing, H.W., Nunoo, S., Niu, S.J., Wang, S.Y., 2015. Evolution of cohesion and friction angle during microfracture accumulation in rock. Nat Hazards 77, 497-510.

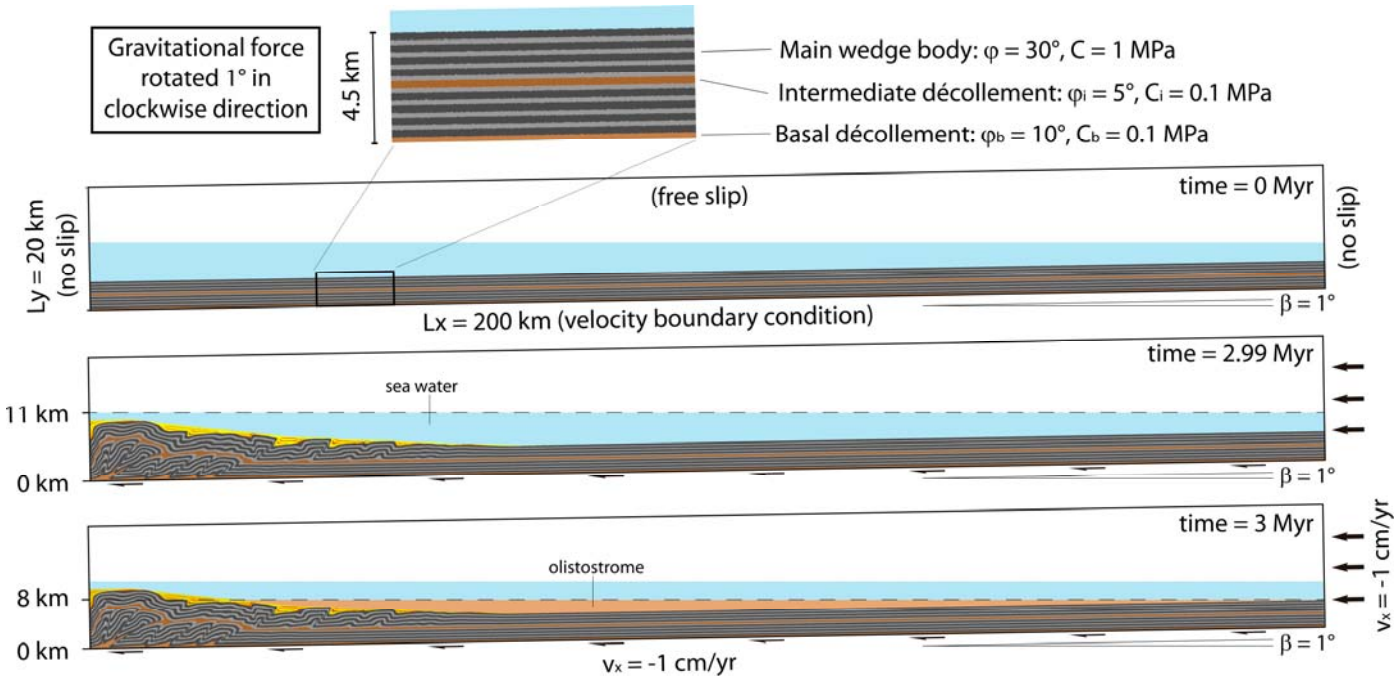

Figure DR1. Model setup. Eulerian box size is 20x200 km in *y*- and *x*-direction, with 200x2000 nodal cells, resulting in a resolution of 100 m in both spatial directions. The gravitational force is rotated clockwise with 1° (g_y = 9.808506 m^2/s and g_x = -0.171208 m^2/s) to mimick an inclination of the wedge base towards the backstop (left). The total initial sedimentary sequence is of 4.5 km, with a basal and an intermediate décollement, each 250 m thick. The water level is at 11 km height at the left boundary (decreasing towards the right at 1°). The olistostrome is emplaced after 3 Myr. The olistostrome surface at its emplacement is at 8 km above the model base at the left boundary (decreasing towards the right at 1°).

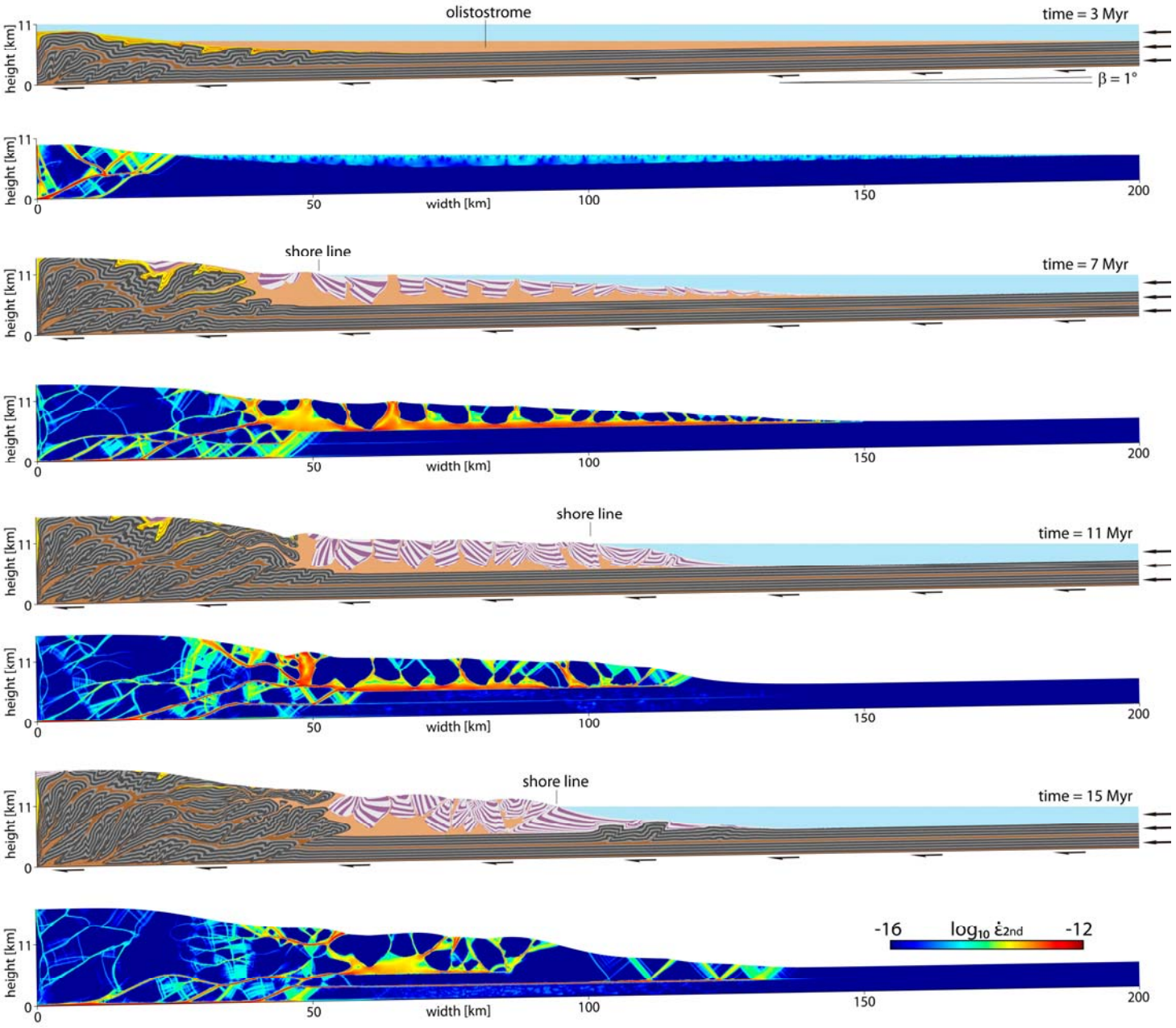

Figure DR2: Temporal evolution of the Model 2 with olistostrome viscosity of η_{olisto} = **5·10^{18} Pa·s**, olistostrome density of ρ_{olisto} = **2000 kg/m^3**, and a surface diffusivity of κ = **10^{-6} m^2/s**. Grey colors: Initial sequence. Brown: Décollements. Yellow/orange: Pre-olistostrome syn-tectonic sediments. Light brown: Olistostrome. Light grey/violet: Post-olistostrome syn-tectonic sediments. Blue: Water.

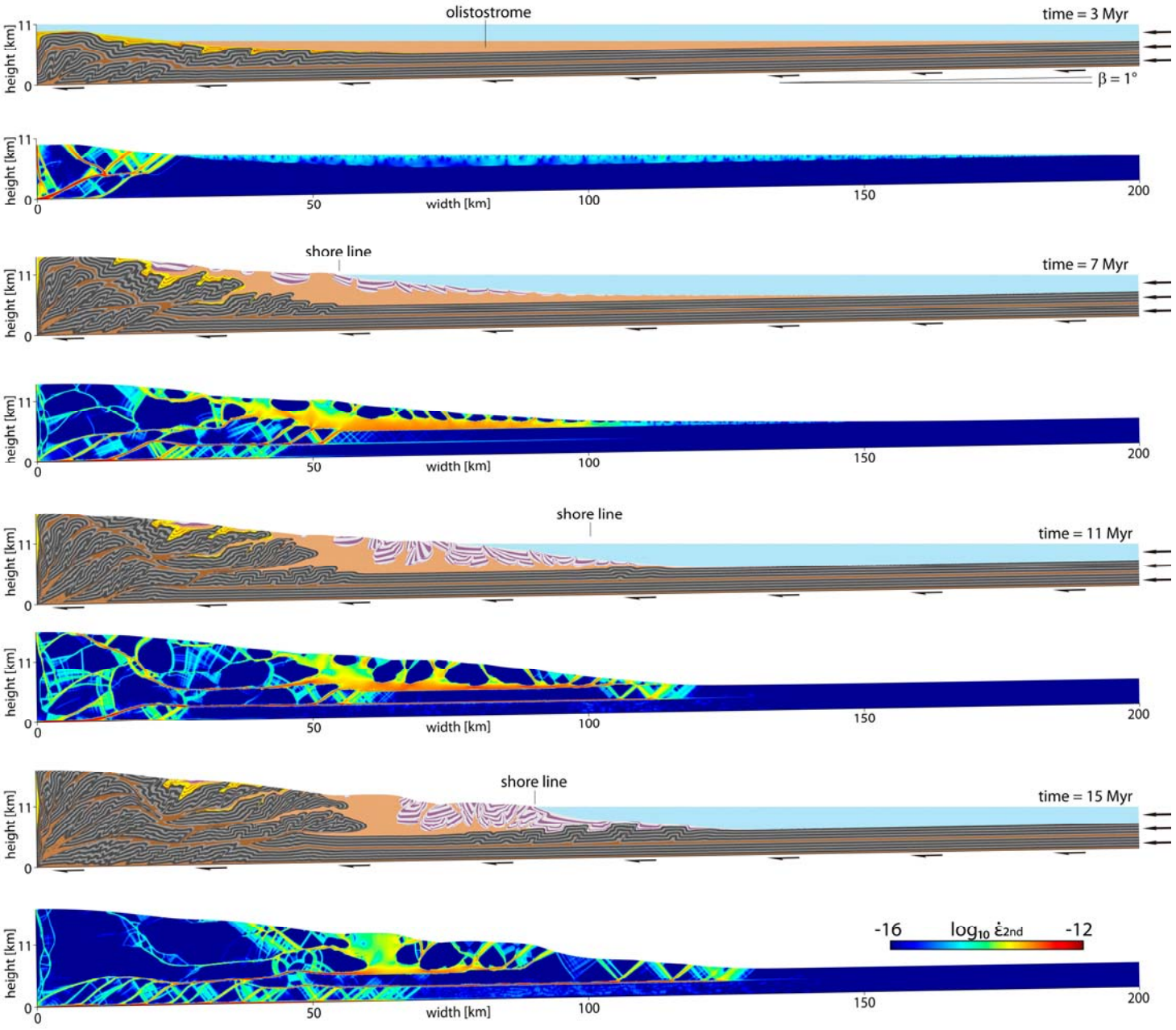

Figure DR3: Temporal evolution of the Model 3 with olistostrome viscosity of η_{olisto} = **2·10^{19} Pa·s**, olistostrome density of ρ_{olisto} = **2000 kg/m^3**, and a surface diffusivity of κ = **10^{-6} m^2/s**. Grey colors: Initial sequence. Brown: Décollements. Yellow/orange: Pre-olistostrome syn-tectonic sediments. Light brown: Olistostrome. Light grey/violet: Post-olistostrome syn-tectonic sediments. Blue: Water.

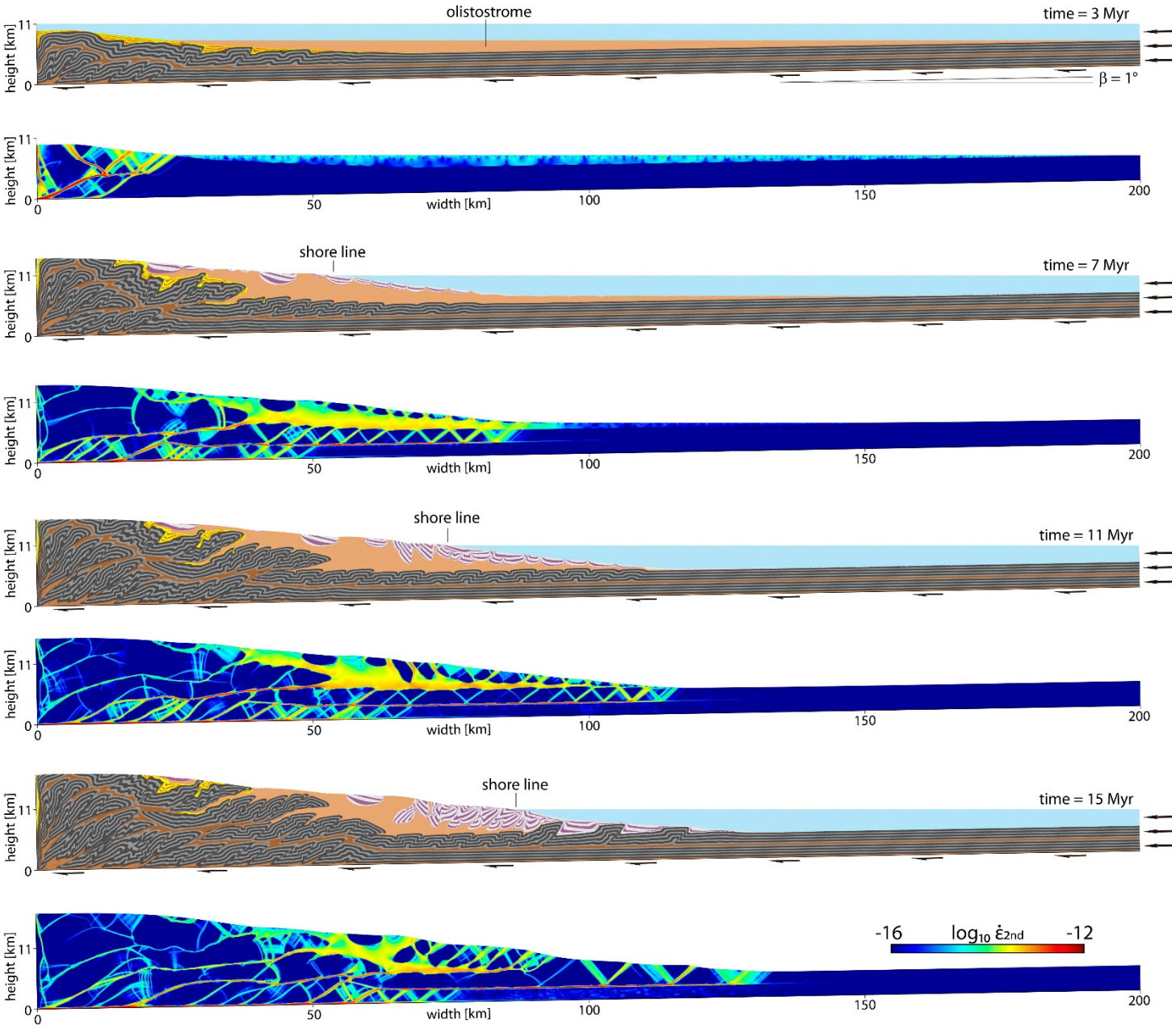

Figure DR4: Temporal evolution of the Model 4 with olistostrome viscosity of $\eta_{olisto} = 5 \cdot 10^{19}$ **Pa·s**, olistostrome density of $\rho_{olisto} = 2000$ **kg/m^3**, and a surface diffusivity of $\kappa = 10^{-6}$ **m^2/s**. Grey colors: Initial sequence. Brown: Décollements. Yellow/orange: Pre-olistostrome syn-tectonic sediments. Light brown: Olistostrome. Light grey/violet: Post-olistostrome syn-tectonic sediments. Blue: Water.

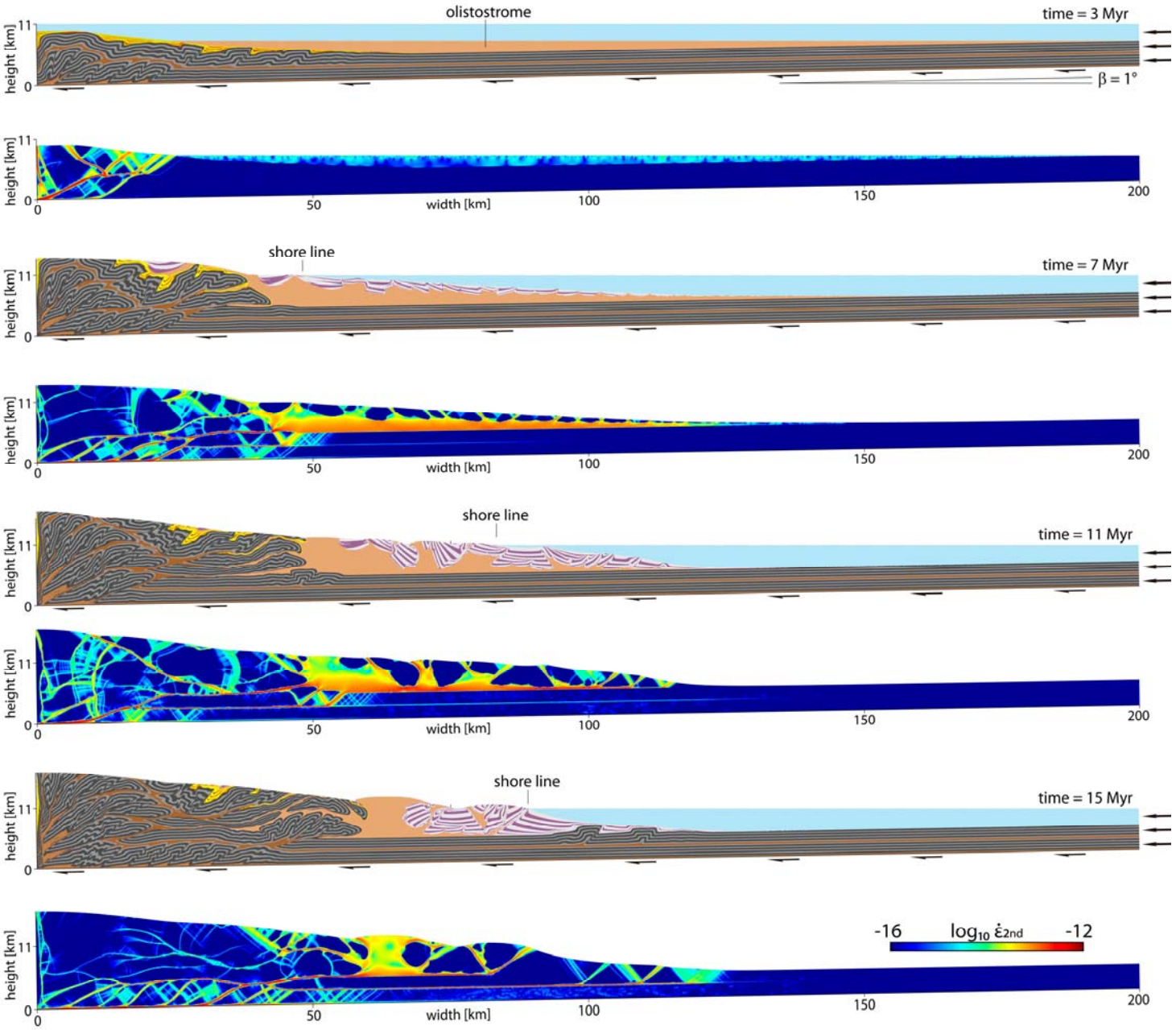

Figure DR5: Temporal evolution of the Model 5 with olistostrome viscosity of η_{olisto} **= 10^{19} Pa·s**, olistostrome density of ρ_{olisto} **= 2200 kg/m^3**, and a surface diffusivity of κ **= 10^{-6} m^2/s**. Grey colors: Initial sequence. Brown: Décollements. Yellow/orange: Pre-olistostrome syn-tectonic sediments. Light brown: Olistostrome. Light grey/violet: Post-olistostrome syn-tectonic sediments. Blue: Water.

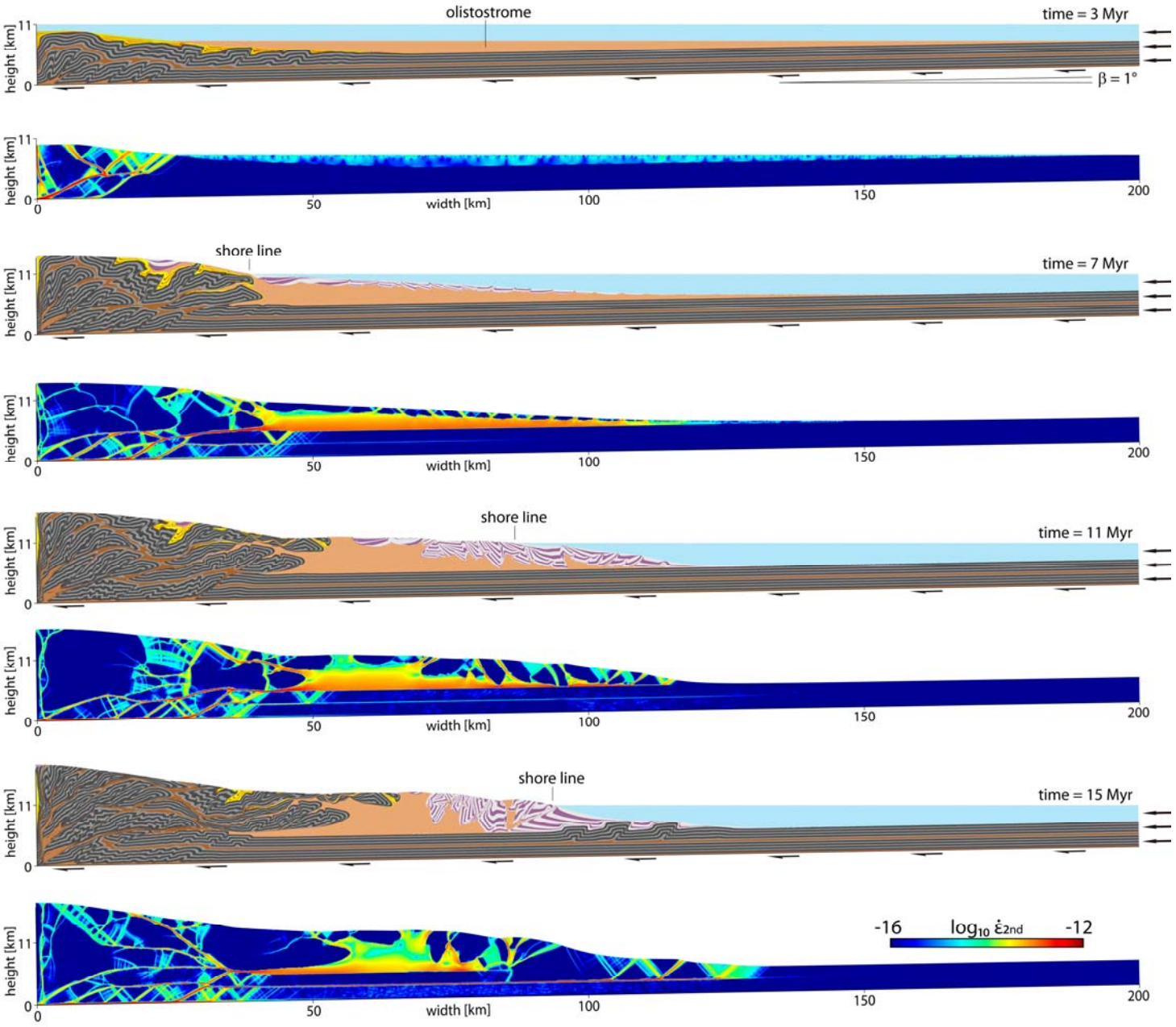

Figure DR6: Temporal evolution of the Model 6 with olistostrome viscosity of η_{olisto} = **10^{19} Pa·s**, olistostrome density of ρ_{olisto} = **2400 kg/m^3**, and a surface diffusivity of κ = **10^{-6} m^2/s**. Grey colors: Initial sequence. Brown: Décollements. Yellow/orange: Pre-olistostrome syn-tectonic sediments. Light brown: Olistostrome. Light grey/violet: Post-olistostrome syn-tectonic sediments. Blue: Water.

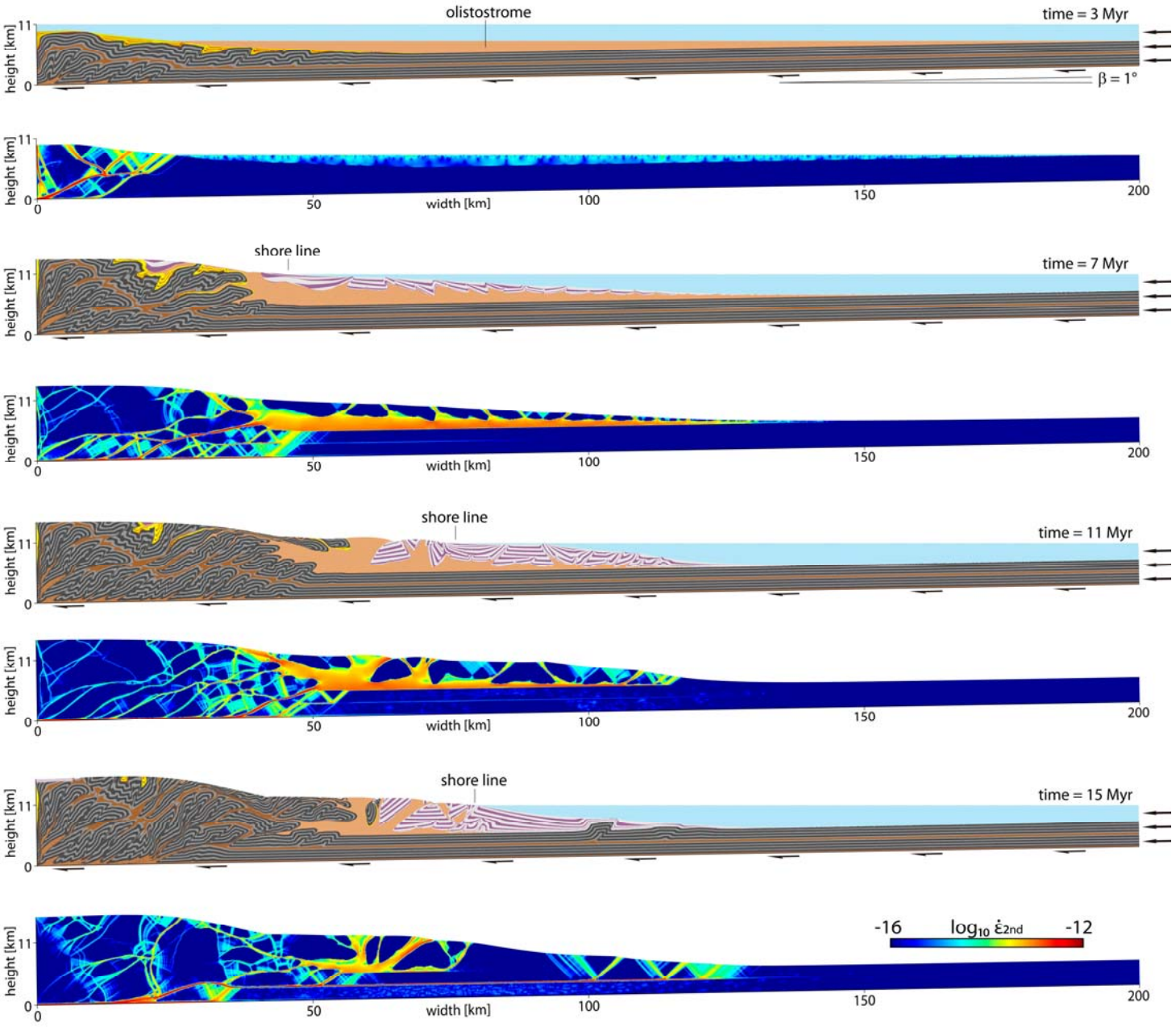

Figure DR7: Temporal evolution of the Model 7 with olistostrome viscosity of η_{olisto} = **10^{19} Pa·s**, olistostrome density of ρ_{olisto} = **2000 kg/m^3**, and a surface diffusivity of κ = **$2 \cdot 10^{-6}$ m^2/s**. Grey colors: Initial sequence. Brown: Décollements. Yellow/orange: Pre-olistostrome syn-tectonic sediments. Light brown: Olistostrome. Light grey/violet: Post-olistostrome syn-tectonic sediments. Blue: Water.

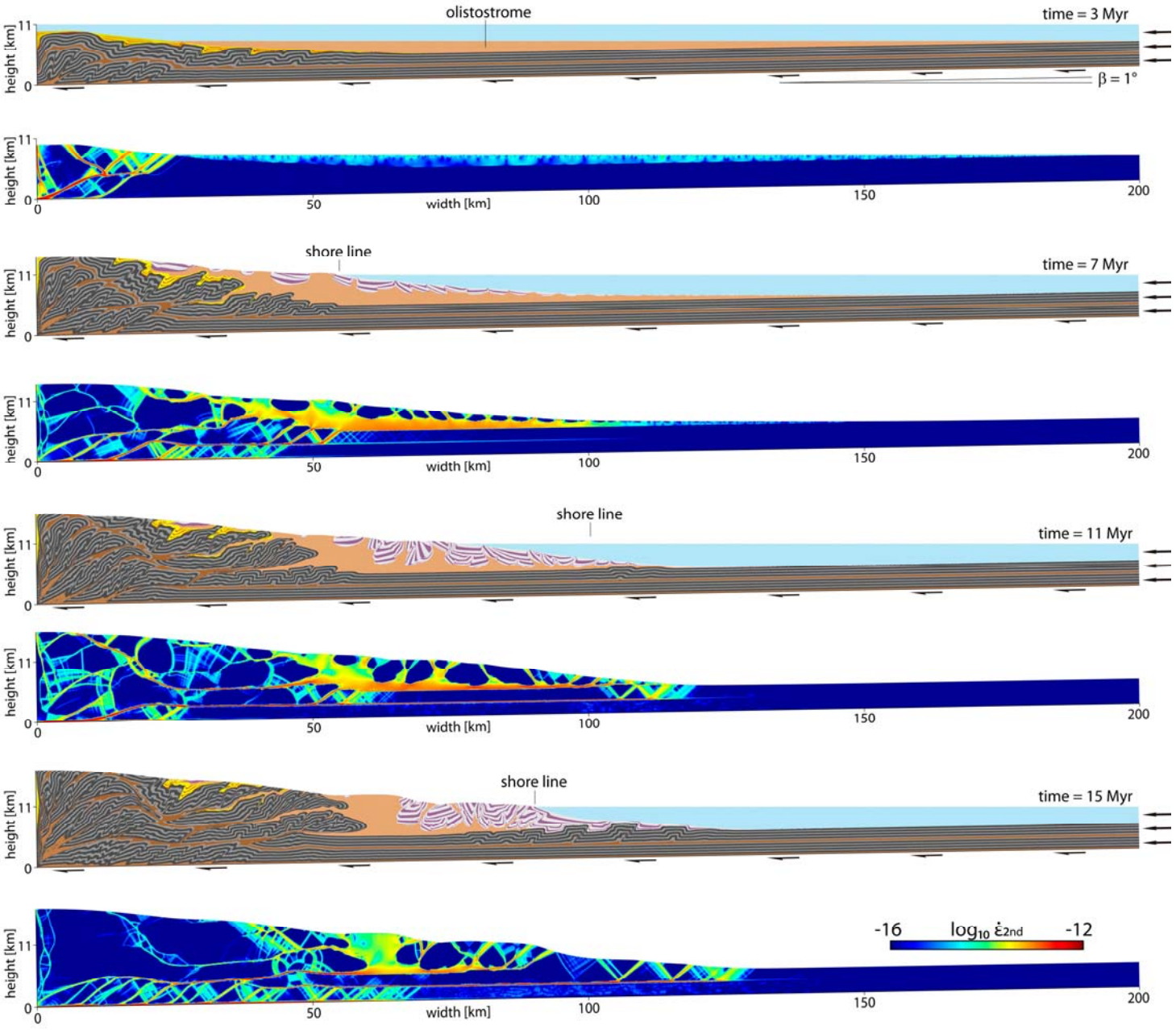

Figure DR8: Temporal evolution of the Model 8 with olistostrome viscosity of η_{olisto} = **10^{19} Pa·s**, olistostrome density of ρ_{olisto} = **2000 kg/m^3**, and a surface diffusivity of κ = **$5 \cdot 10^{-6}$ m^2/s**. Grey colors: Initial sequence. Brown: Décollements. Yellow/orange: Pre-olistostrome syn-tectonic sediments. Light brown: Olistostrome. Light grey/violet: Post-olistostrome syn-tectonic sediments. Blue: Water.

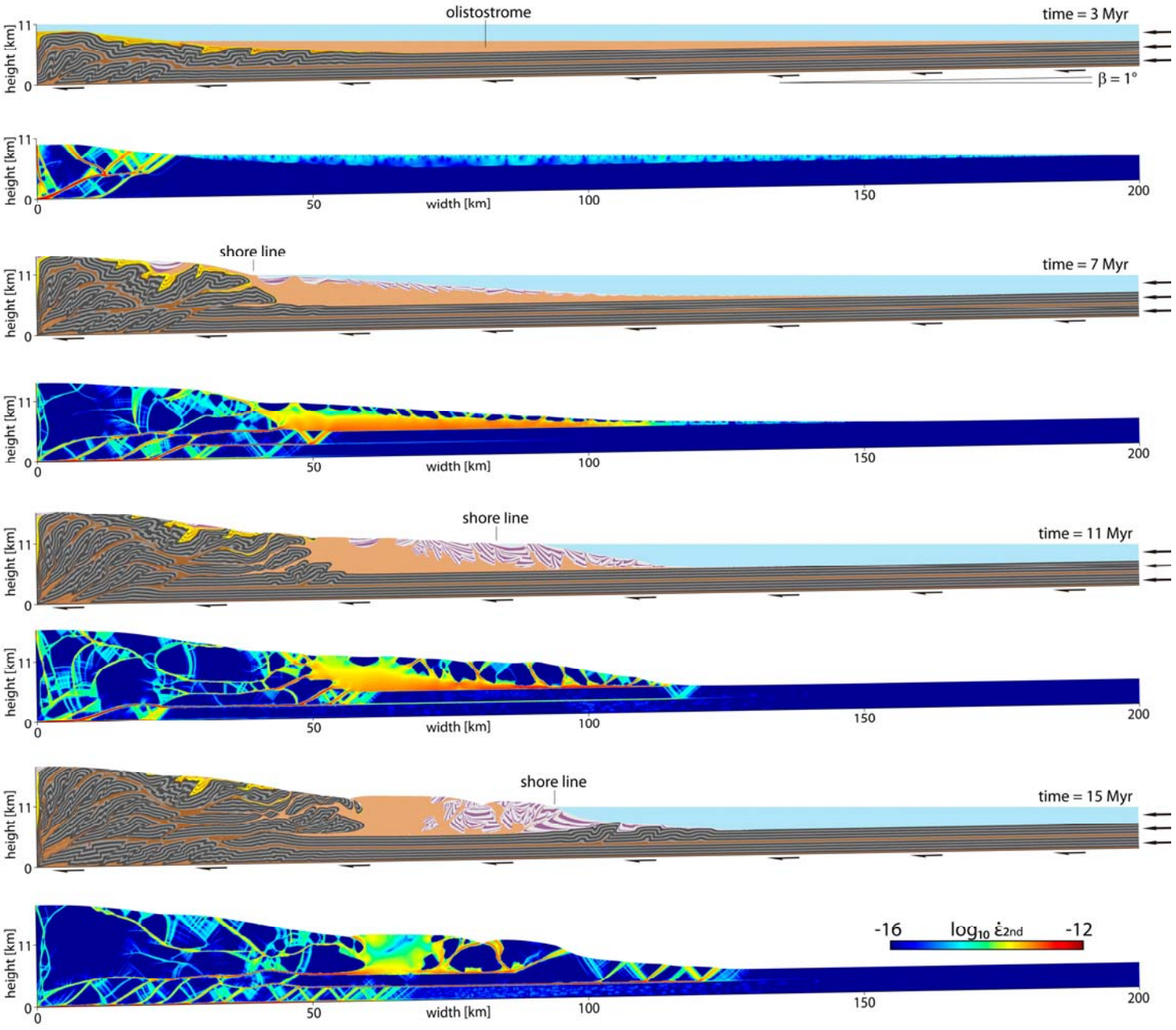

Figure DR9: Temporal evolution of the Model 9 with olistostrome viscosity of η_{olisto} = **10^{19} Pa·s**, olistostrome density of ρ_{olisto} = **2200 kg/m^3**, and a surface diffusivity of κ = **$5 \cdot 10^{-7}$ m^2/s**. Grey colors: Initial sequence. Brown: Décollements. Yellow/orange: Pre-olistostrome syn-tectonic sediments. Light brown: Olistostrome. Light grey/violet: Post-olistostrome syn-tectonic sediments. Blue: Water.

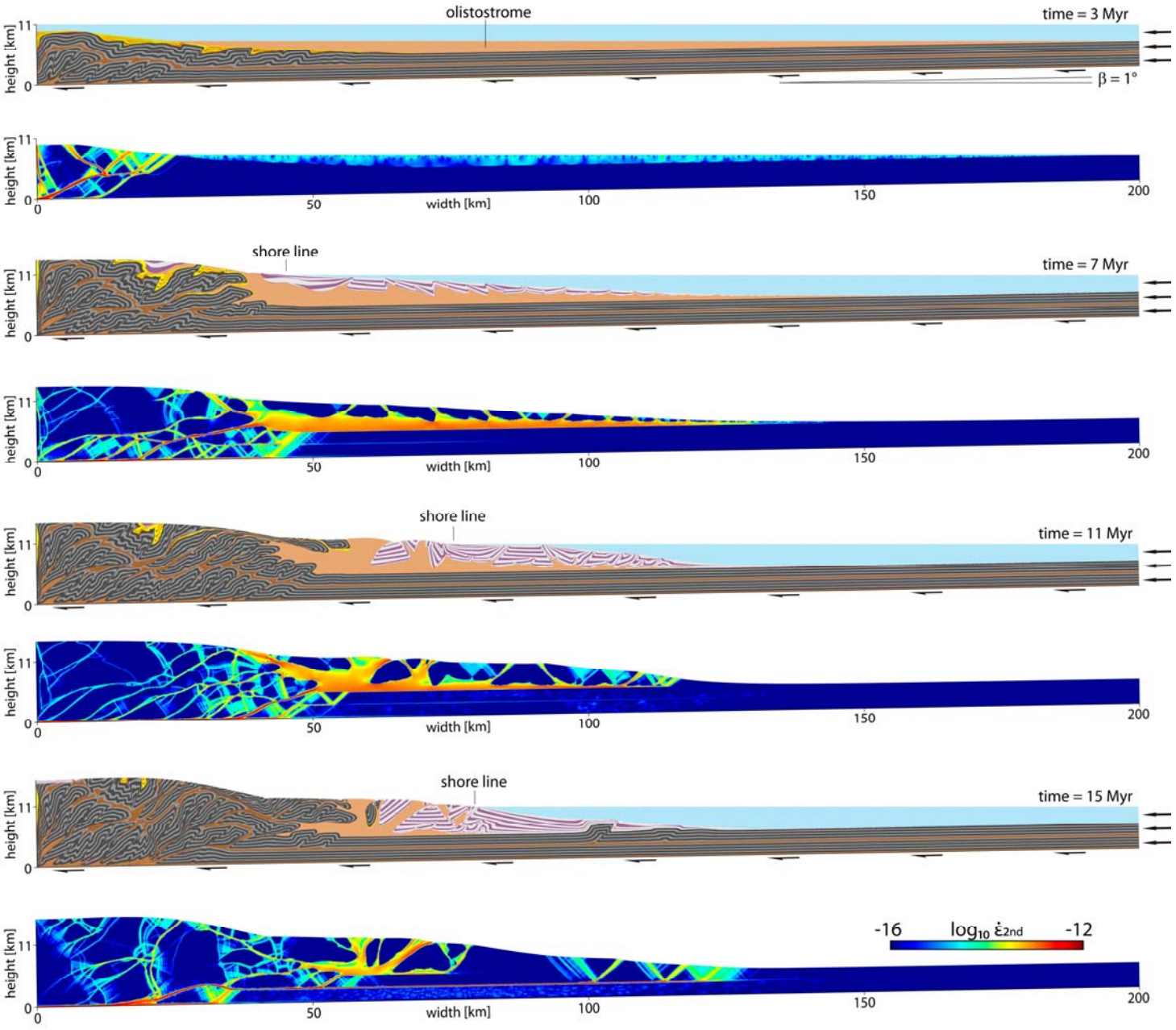

Figure DR10: Temporal evolution of the Model 10 with olistostrome viscosity of η_{olisto} = **10^{19} Pa·s**, olistostrome density of ρ_{olisto} = **2200 kg/m^3**, and a surface diffusivity of κ = **$2 \cdot 10^{-6}$ m^2/s**. Grey colors: Initial sequence. Brown: Décollements. Yellow/orange: Pre-olistostrome syn-tectonic sediments. Light brown: Olistostrome. Light grey/violet: Post-olistostrome syn-tectonic sediments. Blue: Water.

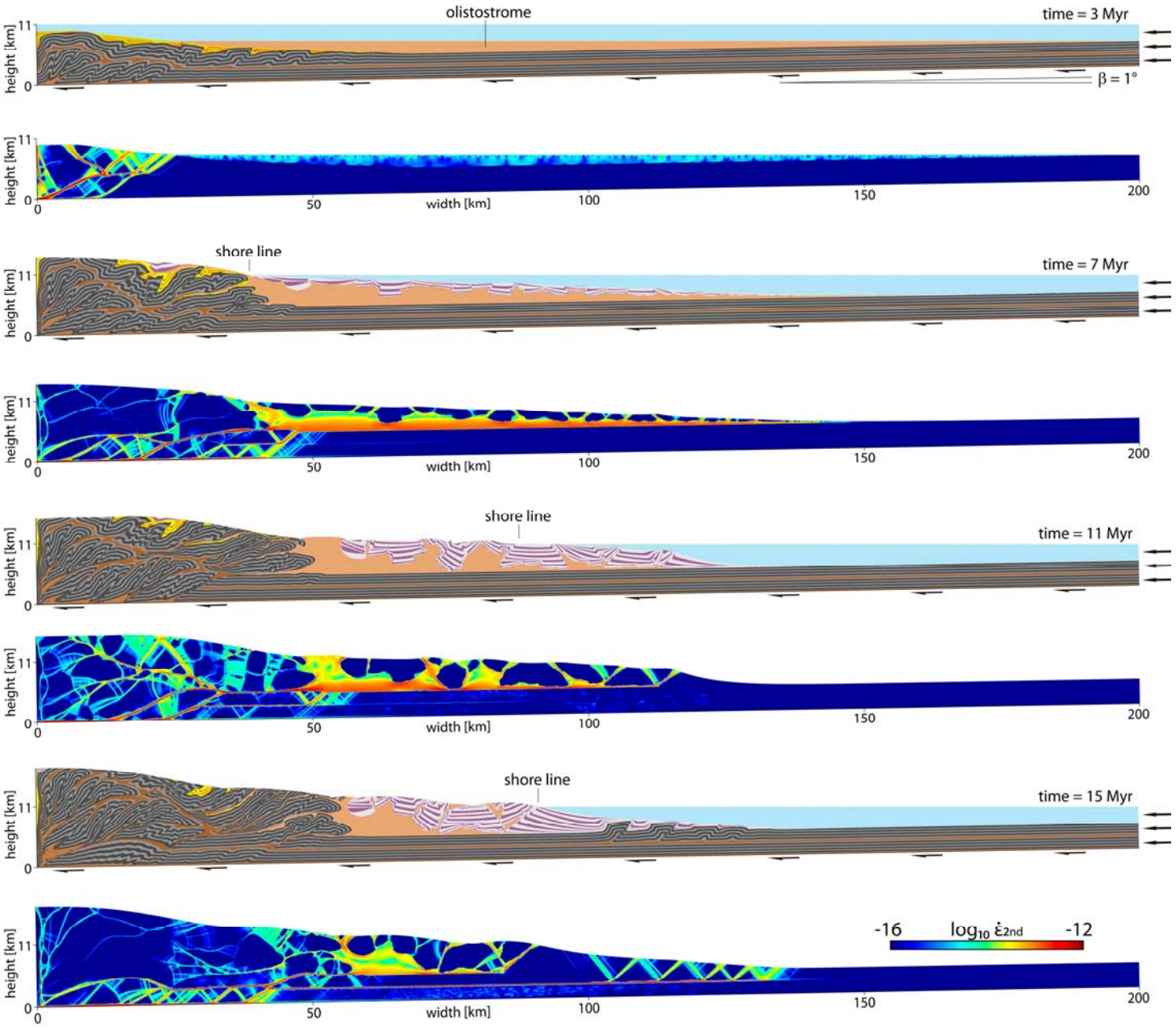

Figure DR11: Temporal evolution of the Model 11 with olistostrome viscosity of $\eta_{olisto} = 5 \cdot 10^{18}$ **Pa·s**, olistostrome density of $\rho_{olisto} = 2200$ **kg/m^3**, and a surface diffusivity of $\kappa = 10^{-6}$ **m^2/s**. Grey colors: Initial sequence. Brown: Décollements. Yellow/orange: Pre-olistostrome syn-tectonic sediments. Light brown: Olistostrome. Light grey/violet: Post-olistostrome syn-tectonic sediments. Blue: Water.

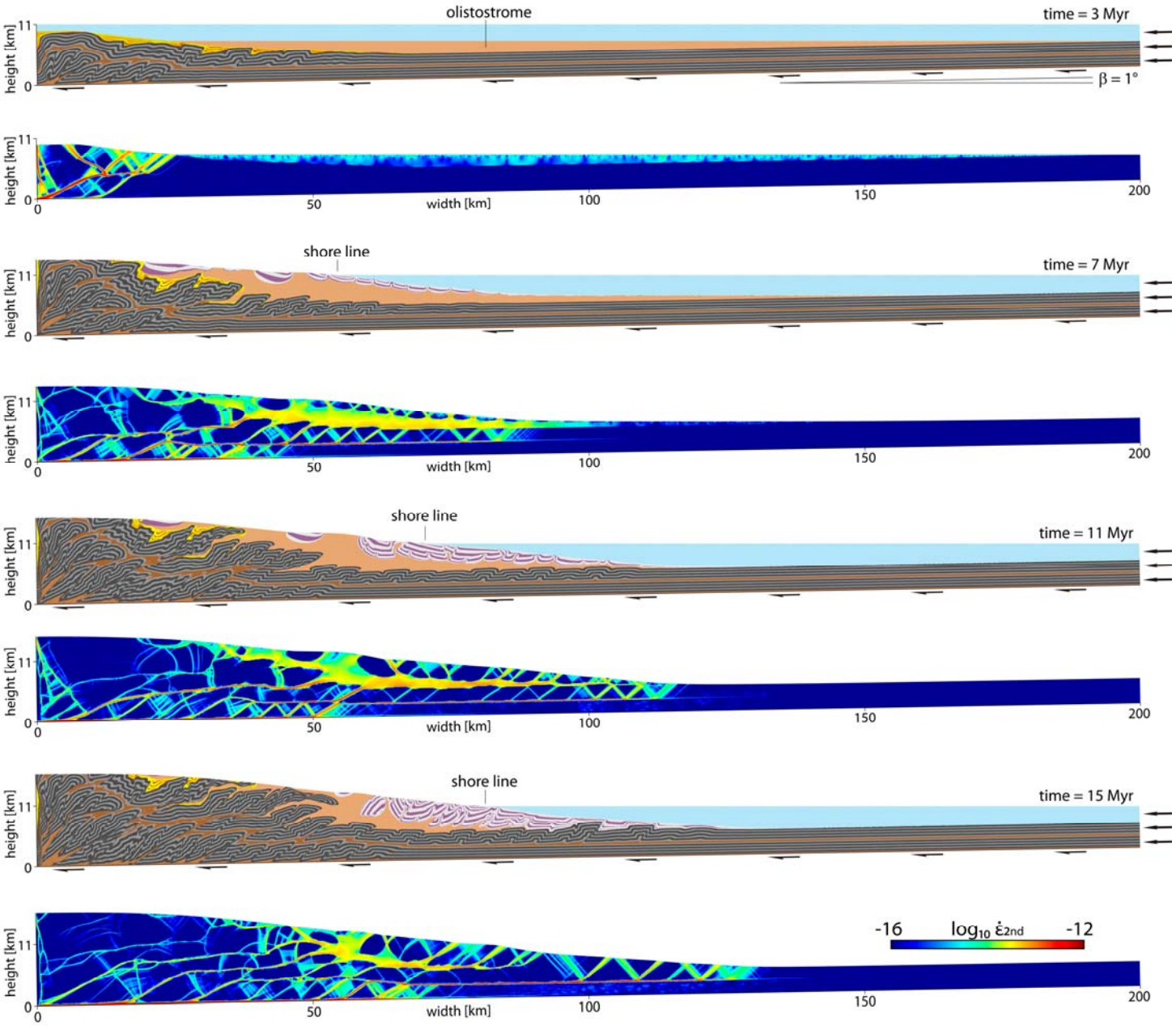

Figure DR12: Temporal evolution of the Model 12 with olistostrome viscosity of $\eta_{olisto} = 5 \cdot 10^{19}$ **Pa·s**, olistostrome density of $\rho_{olisto} = 2200$ **kg/m^3**, and a surface diffusivity of $\kappa = 10^{-6}$ **m^2/s**. Grey colors: Initial sequence. Brown: Décollements. Yellow/orange: Pre-olistostrome syn-tectonic sediments. Light brown: Olistostrome. Light grey/violet: Post-olistostrome syn-tectonic sediments. Blue: Water.

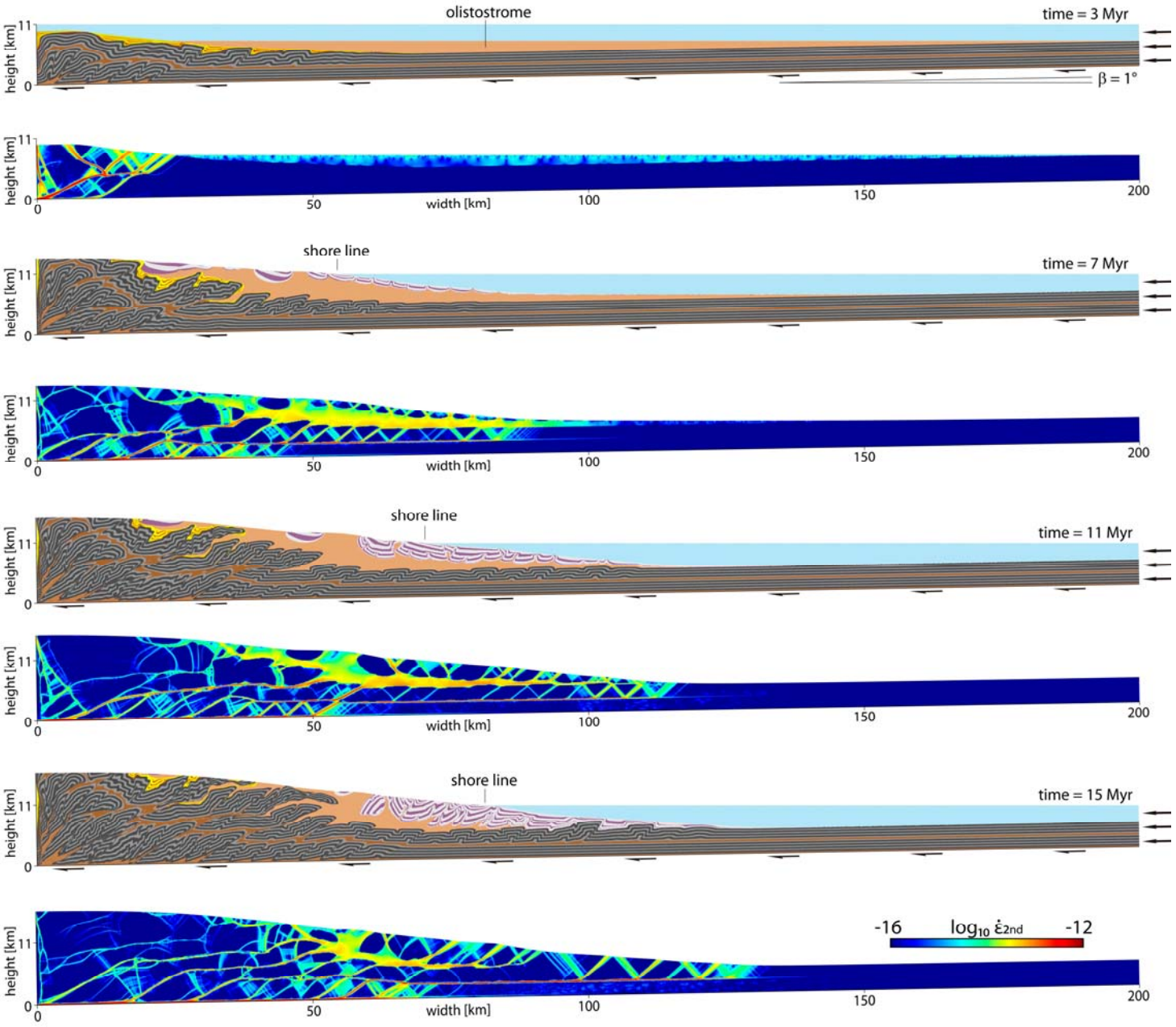

Figure DR13: Temporal evolution of the Model 13 with olistostrome viscosity of η_{olisto} = **2·10^{19} Pa·s**, olistostrome density of ρ_{olisto} = **2000 kg/m^3**, and a surface diffusivity of κ = **2·10^{-6} m^2/s**. Grey colors: Initial sequence. Brown: Décollements. Yellow/orange: Pre-olistostrome syn-tectonic sediments. Light brown: Olistostrome. Light grey/violet: Post-olistostrome syn-tectonic sediments. Blue: Water.

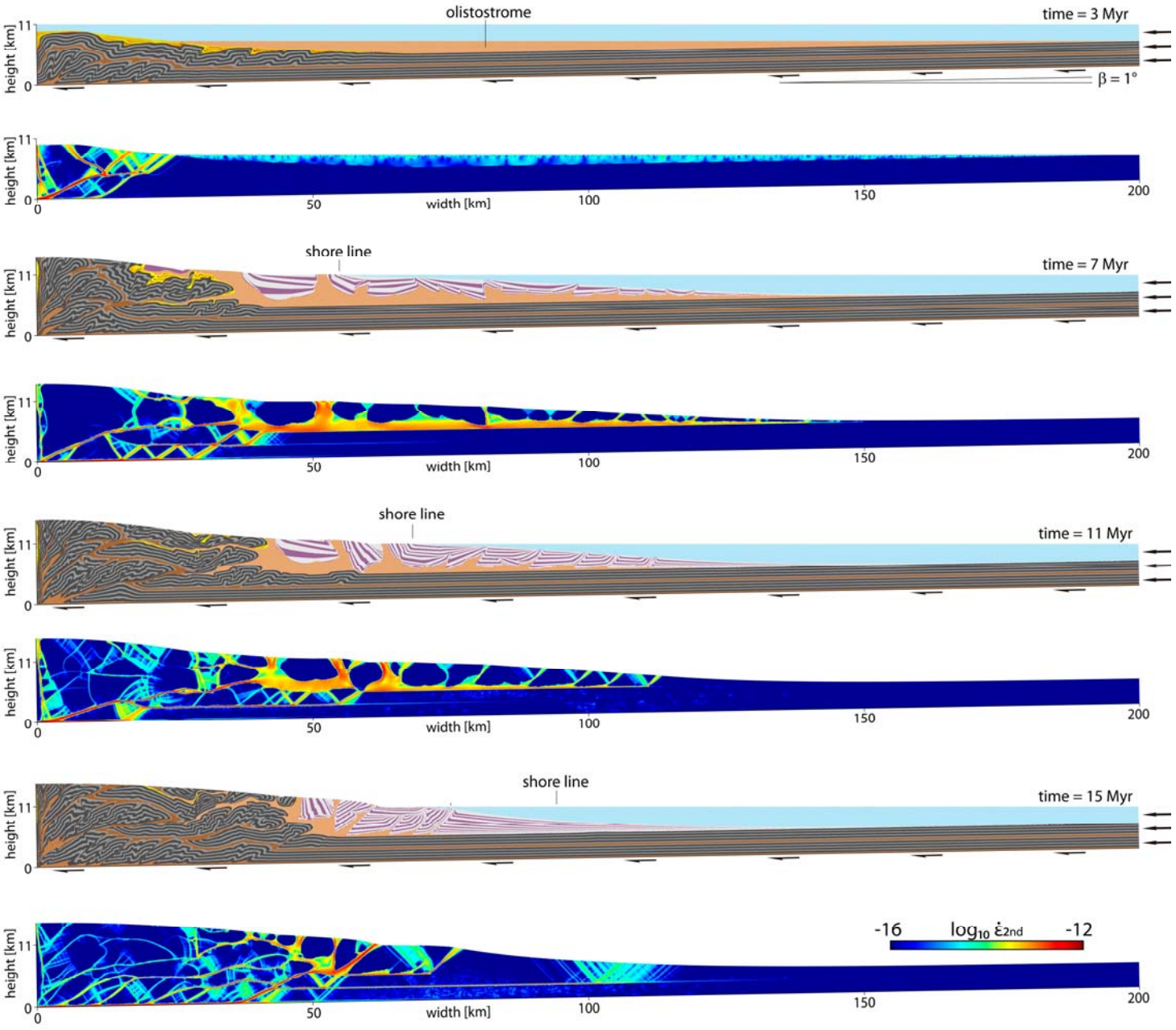

Figure DR14: Temporal evolution of the Model 14 with olistostrome viscosity of $\eta_{olisto} = 2 \cdot 10^{19}$ **Pa·s**, olistostrome density of $\rho_{olisto} = 2000$ **kg/m^3**, and a surface diffusivity of $\kappa = 5 \cdot 10^{-6}$ **m^2/s**. Grey colors: Initial sequence. Brown: Décollements. Yellow/orange: Pre-olistostrome syn-tectonic sediments. Light brown: Olistostrome. Light grey/violet: Post-olistostrome syn-tectonic sediments. Blue: Water

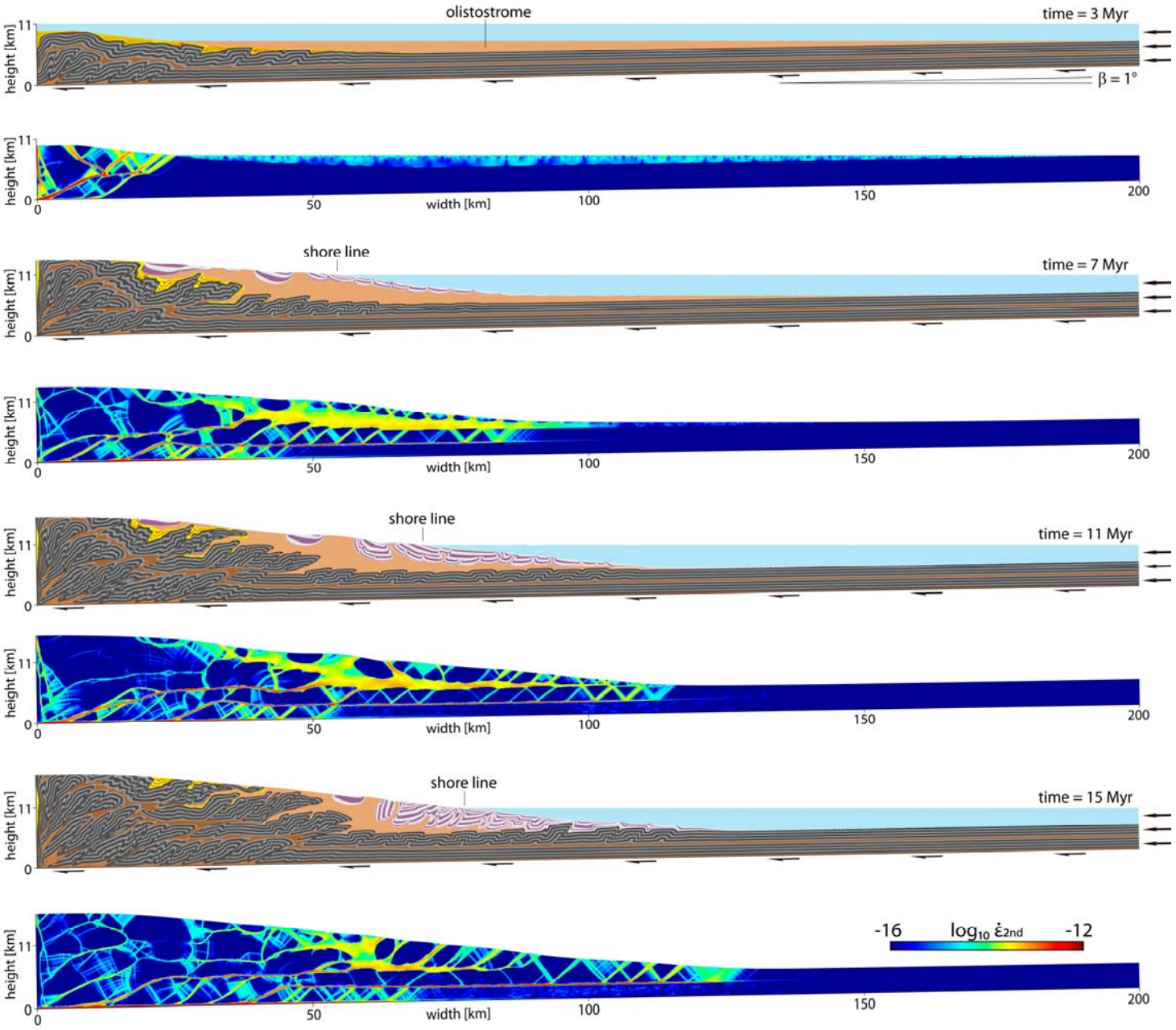

Figure DR15: Temporal evolution of the Model 15 with olistostrome viscosity of η_{olisto} **= 5·10^{19} Pa·s**, olistostrome density of ρ_{olisto} **= 2000 kg/m^3**, and a surface diffusivity of κ **= 2·10^{-6} m^2/s**. Grey colors: Initial sequence. Brown: Décollements. Yellow/orange: Pre-olistostrome syn-tectonic sediments. Light brown: Olistostrome. Light grey/violet: Post-olistostrome syn-tectonic sediments. Blue: Water

Table DR1. Properties of olistostrome formation

	Models presented in this study	Values from literature	Material	Literature
Viscosity (Pa.s)	5e18-5e19	1e18	Mobile shales	Albertz et al., 2010
		5e18	Mobile shales	Ings and Beaumont, 2010
Density (kg/m^3)	2000-2400	ca. 1800-2400	Debris flows [a,b]	Mulder and Alexanter, 2001
		ca. 2000	Debris flows [a,b]	Hampton, 1972
		ca. 1700-2300	Overpressured shales [a]	Butler and Baldwin, 1985

[a] Grain density = 2600 kg/m^3

[b] Calculated from sediment concentration

Albertz, M., Beaumont, C., and Ings, S. J., 2010, Geodynamic Modeling of Sedimentation-induced Overpressure, Gravitational Spreading, and Deformation of Passive Margin Mobile Shale Basins, in Wood, L., ed., Shale tectonics, Volume 93, AAPG, p. 29-62.

Baldwin, B., and Butler, C. O., 1985, Compaction Curves: Aapg Bulletin-American Association of Petroleum Geologists, v. 69, no. 4, p. 622-626.

Hampton, M. A., 1972, Role of Subaqueous Debris Flow in Generating Turbidity Currents: Journal of Sedimentary Petrology, v. 42, no. 4, p. 775-793.

Ings, S. J., and Beaumont, C., 2010, Continental margin shale tectonics: preliminary results from coupled fluid-mechanical models of large-scale delta instability: Journal of the Geological Society, v. 167, no. 3, p. 571-582.

Mulder, T., and Alexander, J., 2001, The physical character of subaqueous sedimentary density flows and their deposits: Sedimentology, v. 48, no. 2, p. 269-299.

Table DR2: Olistostrome properties and surface process

	olistostrome viscosity (Pa·s)	olistostrome density (kg/m^3)	surface diffusion (m^2/s)	figure
Model 1 [a]	10^{19}	2000	10^{-6}	3
Model 2	$5{\cdot}10^{18}$	2000	10^{-6}	4, S2
Model 3	$2{\cdot}10^{19}$	2000	10^{-6}	S3
Model 4	$5{\cdot}10^{19}$	2000	10^{-6}	4, S4
Model 5	10^{19}	2200	10^{-6}	S5
Model 6	10^{19}	2400	10^{-6}	4, S6
Model 7	10^{19}	2000	$2{\cdot}10^{-6}$	S7
Model 8	10^{19}	2000	$5{\cdot}10^{-6}$	4, S8
Model 9	10^{19}	2200	$5{\cdot}10^{-7}$	S9
Model 10	10^{19}	2200	$2{\cdot}10^{-6}$	S10
Model 11	$5{\cdot}10^{18}$	2200	10^{-6}	S11
Model 12	$5{\cdot}10^{19}$	2200	10^{-6}	S12
Model 13	$2{\cdot}10^{19}$	2000	$2{\cdot}10^{-6}$	S13
Model 14	$2{\cdot}10^{19}$	2000	$5{\cdot}10^{-6}$	S14
Model 15	$5{\cdot}10^{19}$	2000	$2{\cdot}10^{-6}$	S15

[a] Reference model